Supplementary Information (SI) for Materials Horizons.

Supporting Information

Stretchable Hierarchical Metal Wire Networks for Neuromorphic Emulation of Nociception and Anti-nociception

Bhupesh Yadav [‡]***, Indrajit Mondal***[‡]***, Manpreet Kaur, Vidhyadhiraja N. S., Giridhar U. Kulkarni****

B. Yadav, I. Mondal, M. Kaur, G. U. Kulkarni

Chemistry and Physics of Materials Unit, Jawaharlal Nehru Centre for Advanced Scientific Research, Bangalore 560064, India.

*E-mail: kulkarni@jncasr.ac.in

Vidhyadhiraja N S

Theoretical Science Unit, Jawaharlal Nehru Centre for Advanced Scientific Research, Bangalore 560064, India.

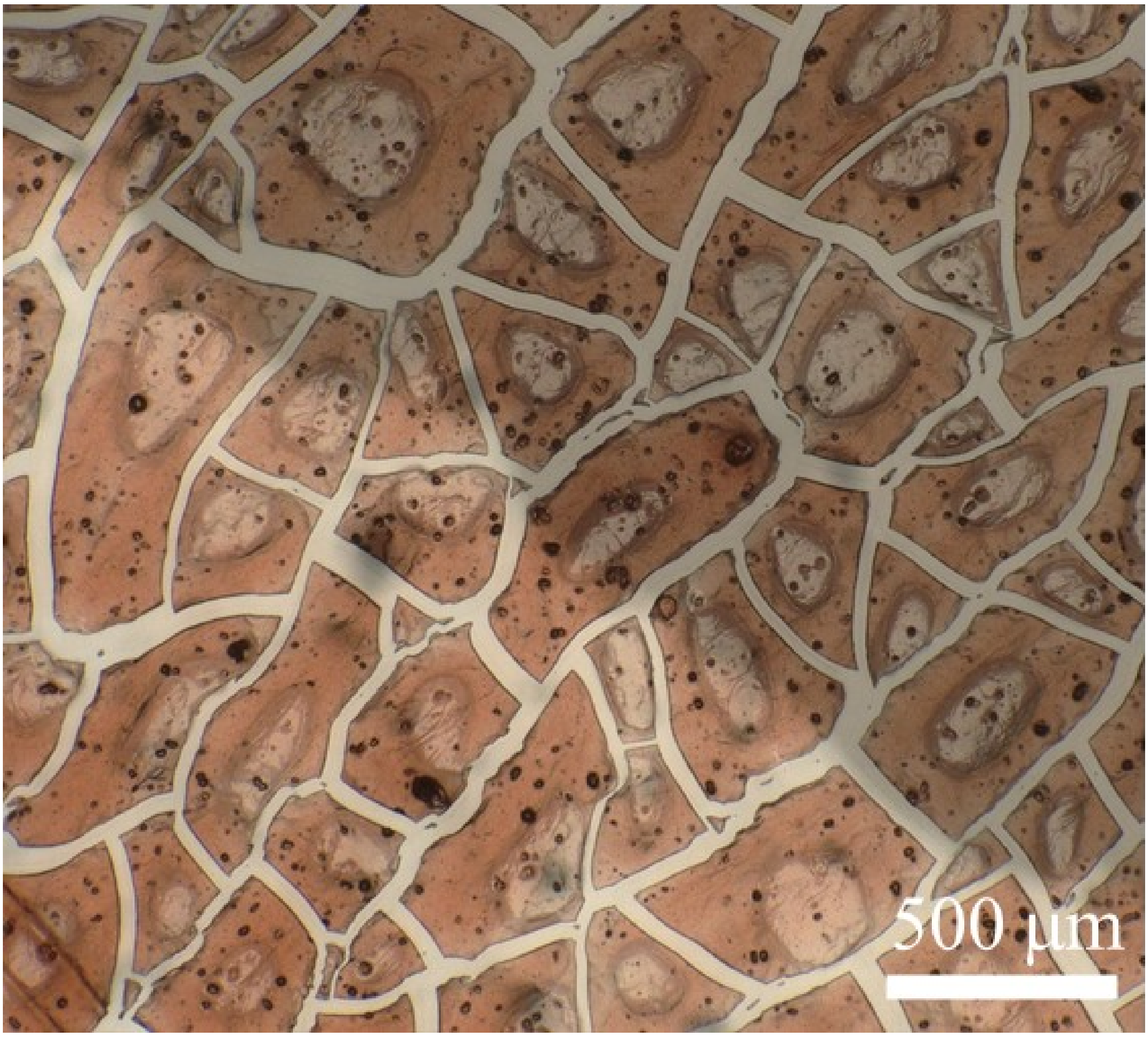

Figure S1. Optical Microscopy image of the micro-crack network achieved after crackle precursor spin coating.

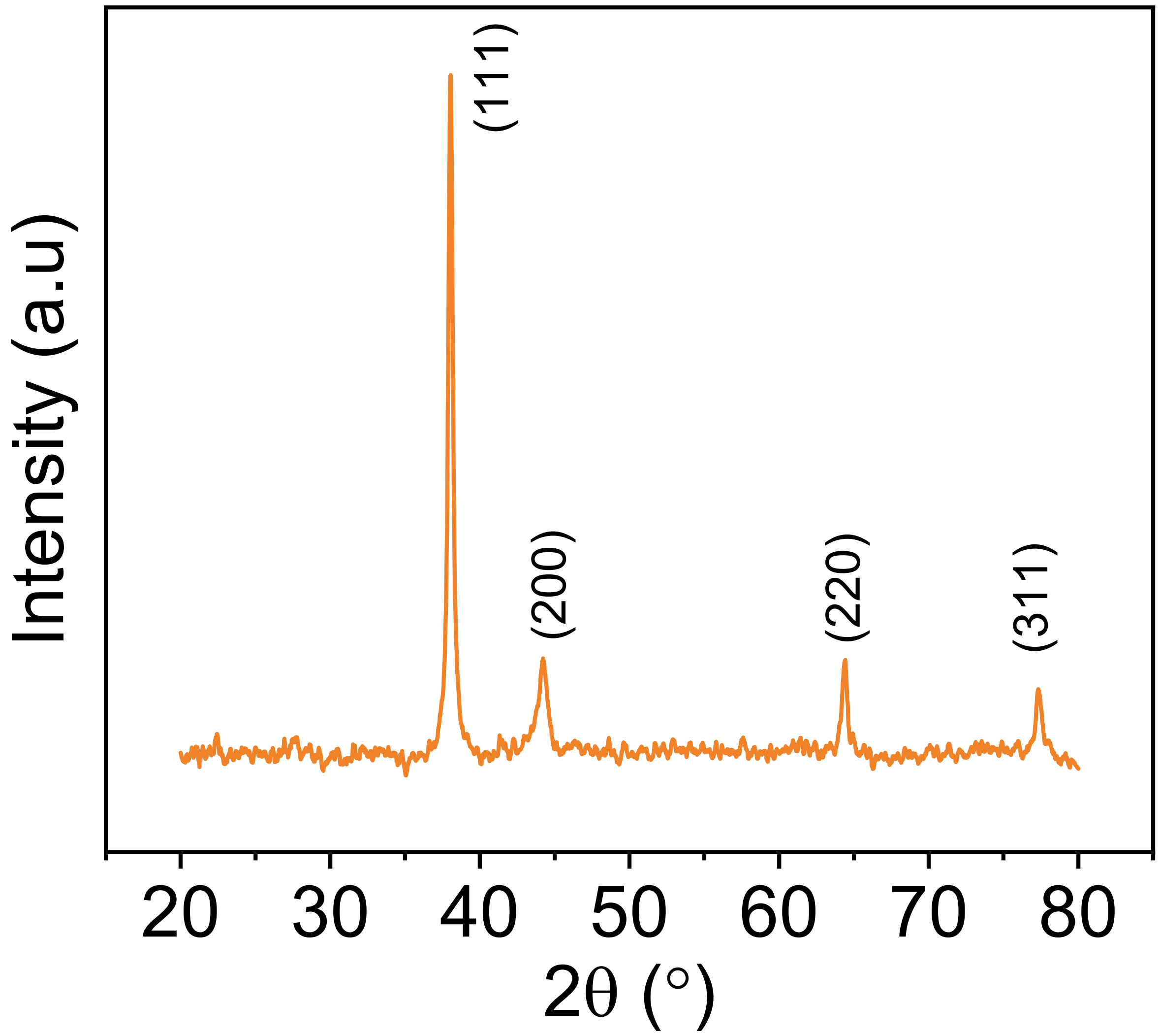

Figure S2. XRD pattern of the micro-channels showing characteristic peaks of Ag.

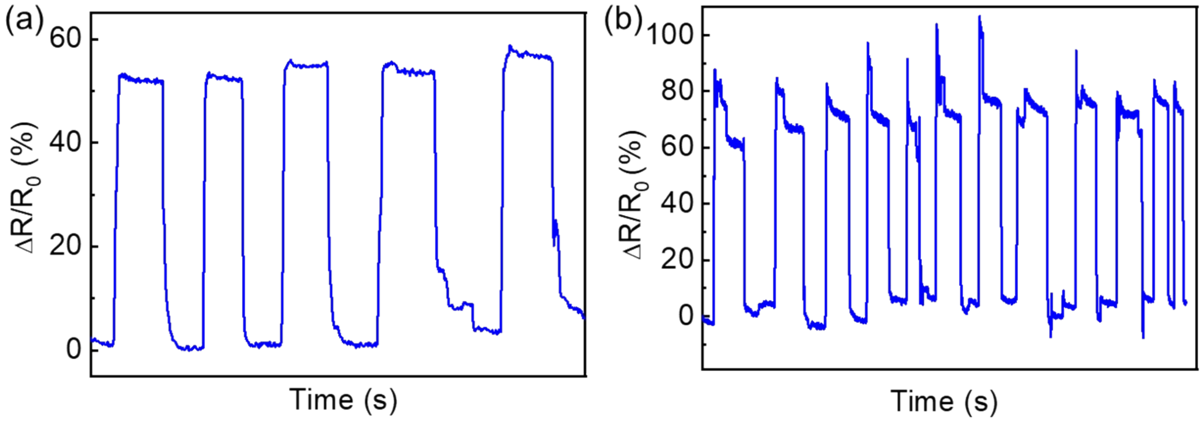

Figure S3. Repeated cycles of resistance change at (a) 0.69% and (b) 1.38% strain.

As seen, the change in resistance is reasonably repeatable. The slight fluctuations at 1.38% strain might be due to the strain value being close to the neuromorphic regime. Additionally, the peaks observed during the application and removal of higher strain are attributed to manual handling of the strain setup, which might have introduced minor inconsistencies.

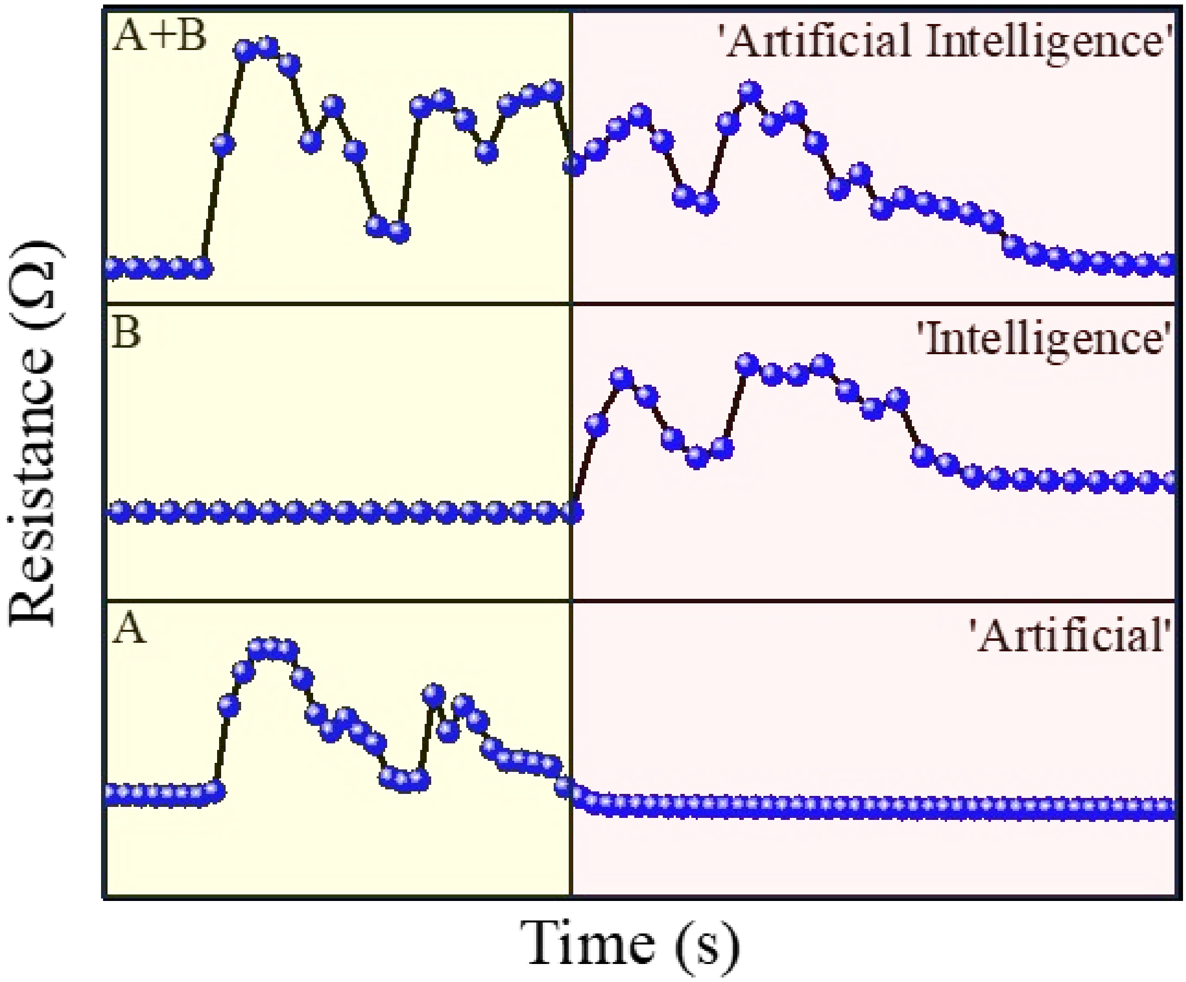

Figure S4. Speech recognition: distinguished resistance pattern generations by the device while playing the words ‘artificial’ (A) and ‘intelligence’ (B) individually and consecutively (A+B) on a cell phone speaker hosting the device, giving rise to (A) + (B) = (A+B).

The device is exploited in speech recognition applications. To demonstrate so, it was mounted on a cell phone speaker to capture the response of spoken words. The aim was to distinctly record the response of two words ‘Artificial (A)’ and ‘Intelligence (B)’ through the resistance change produced in the device. A constant voltage bias was employed by a source meter to record the resistance change. Initially, the word ‘Artificial’ (represented by A) was played and the intricate resistance change produced by the word was recorded. Next, the word ‘intelligence’ (represented by B) was played and recorded in a similar manner. Finally, both the words were played consecutively, and it produced the sum of the patterns produced by A and B.

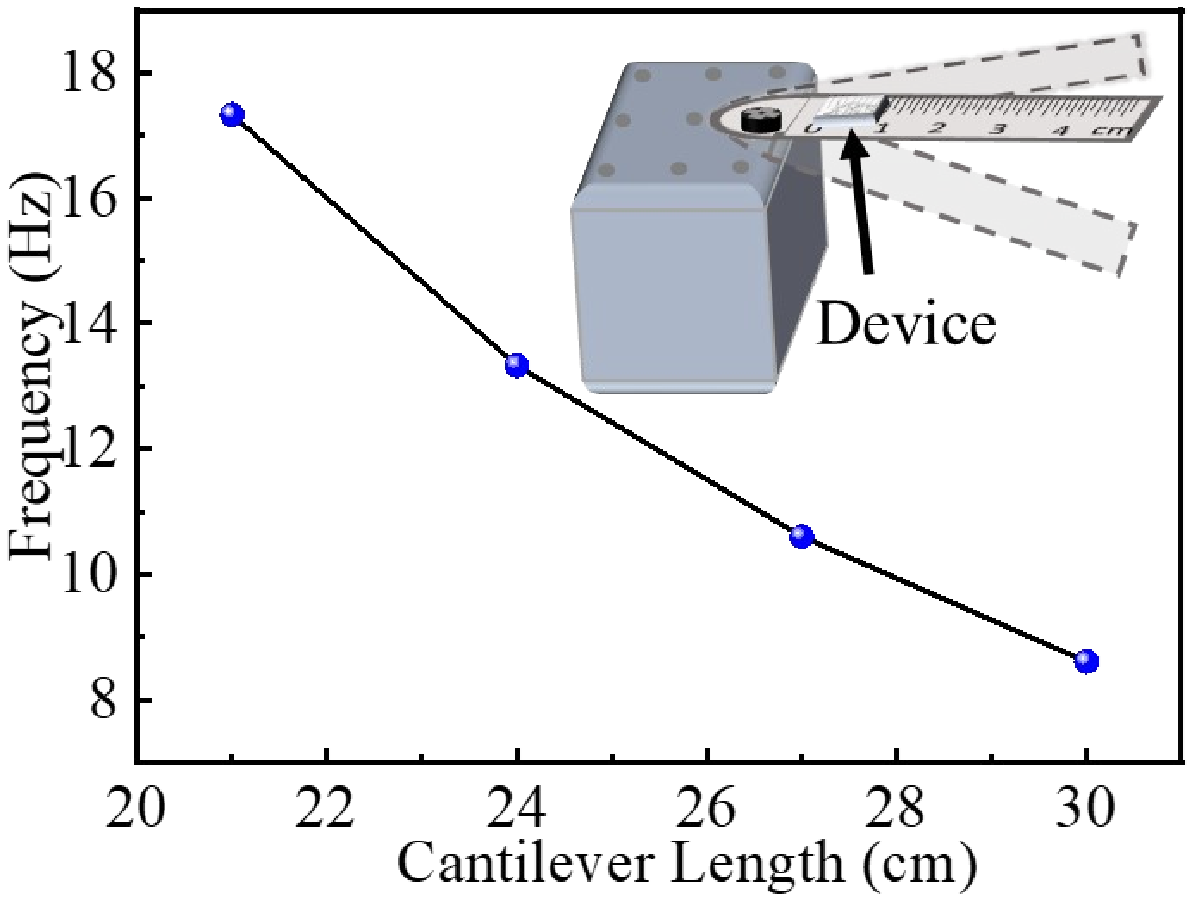

Figure S5. Mechanical frequency detection: precise identification of the length-dependent natural frequency of a cantilever subjected to mechanical vibration. The inset shows a schematic of the experimental setup where the device is placed on a cantilever.

To perform cantilever frequency detection, the device was mounted on a one-edge clamped cantilever (sturdy steel scale) (as shown in the inset of Figure S5) and a deflection was induced to the free end resulted in a damped oscillation that in turn, gives rise to resistance change in the device (see Figure S6). As the cantilever length varied systematically, it gave rise to distinct frequencies each corresponding to a different cantilever length as depicted in Figure S5. All the corresponding curves used for the frequency calculation are shown in Figure S6-S9.

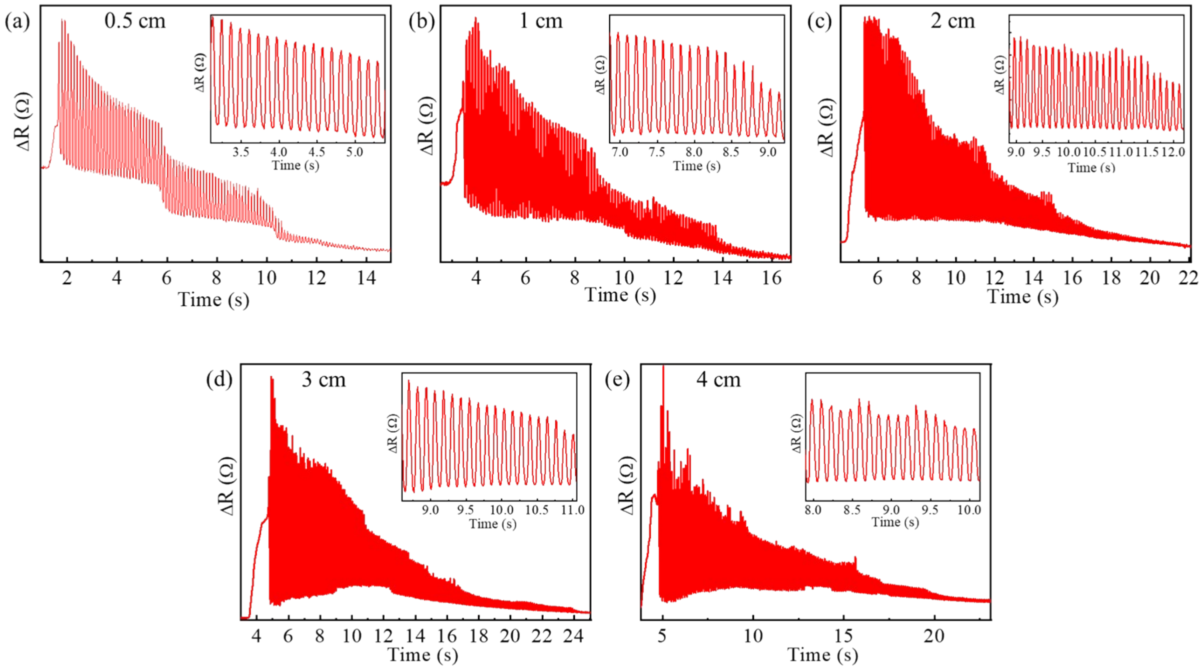

Figure S6. Response of a sensor to damped oscillations of a 30 cm cantilever with initial deflection of (a) 0.5, (b) 1, (c) 2, (d) 3, and (e) 4 cm. Insets are the corresponding enlarged oscillation patterns.

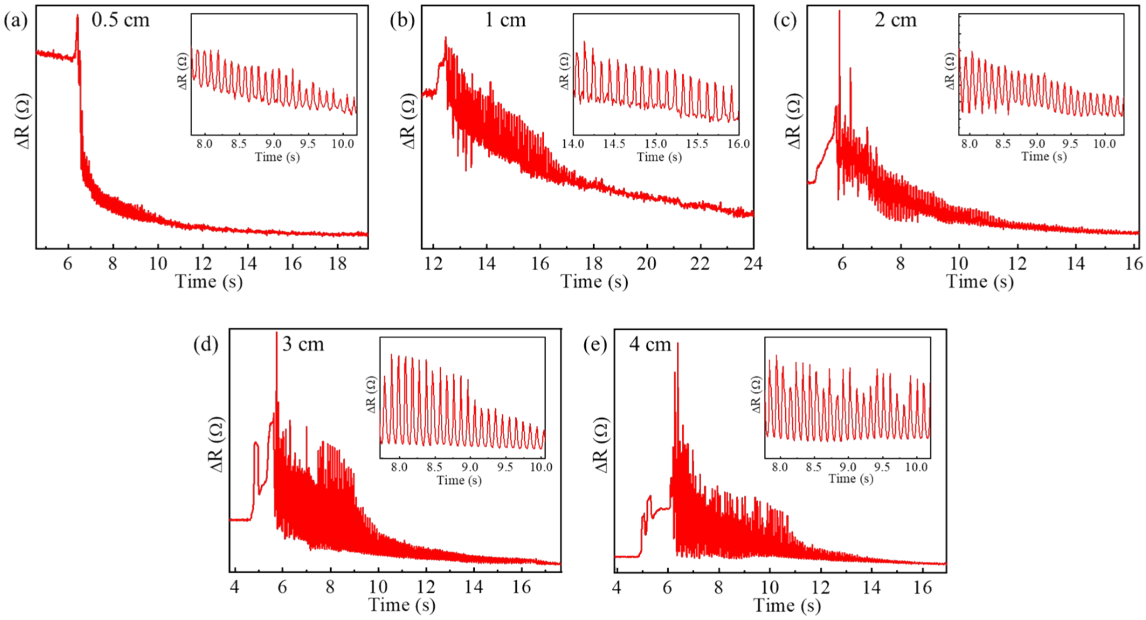

Figure S7. Response of the sensor to damped oscillations of the cantilever with initial deflection of (a) 0.5, (b) 1, (c) 2, (d) 3, and (e) 4 cm while hosting the sensor at a distance of 27 cm from the clamped edge. Insets are the corresponding enlarged oscillation patterns.

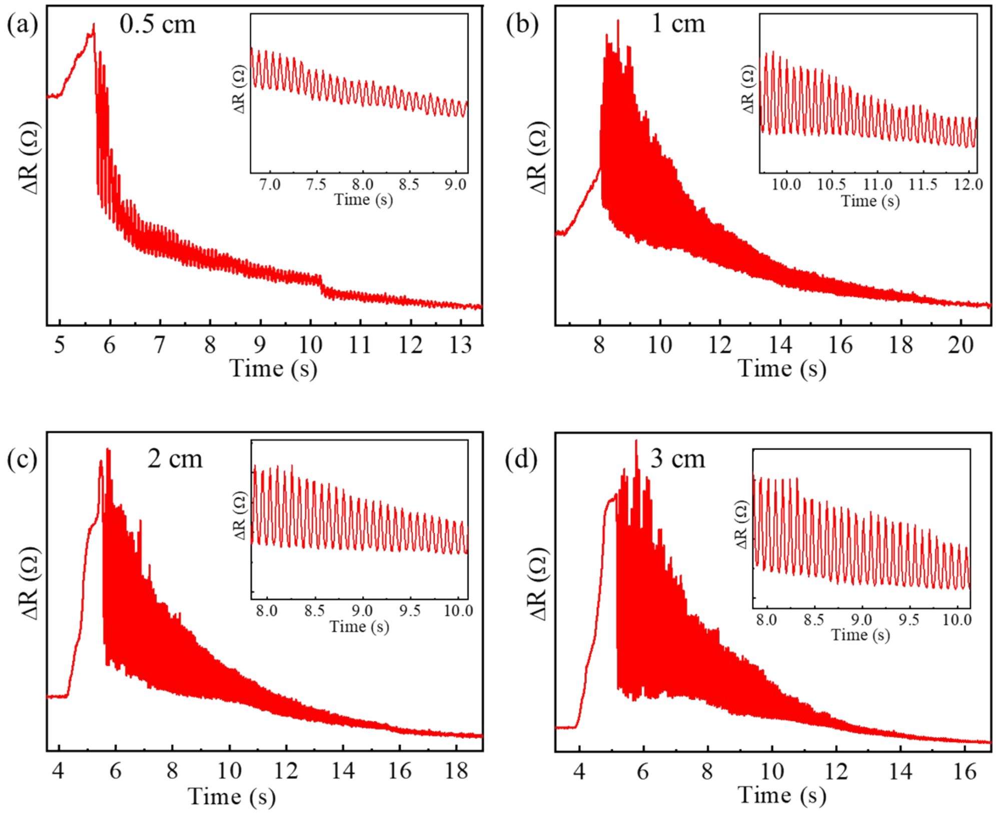

Figure S8. Response of the sensor to damped oscillations of the cantilever with initial deflection of (a) 0.5, (b) 1, (c) 2 and (d) 3 cm while hosting the sensor at a distance of 24 cm from the clamped edge. Insets are the corresponding enlarged oscillation patterns.

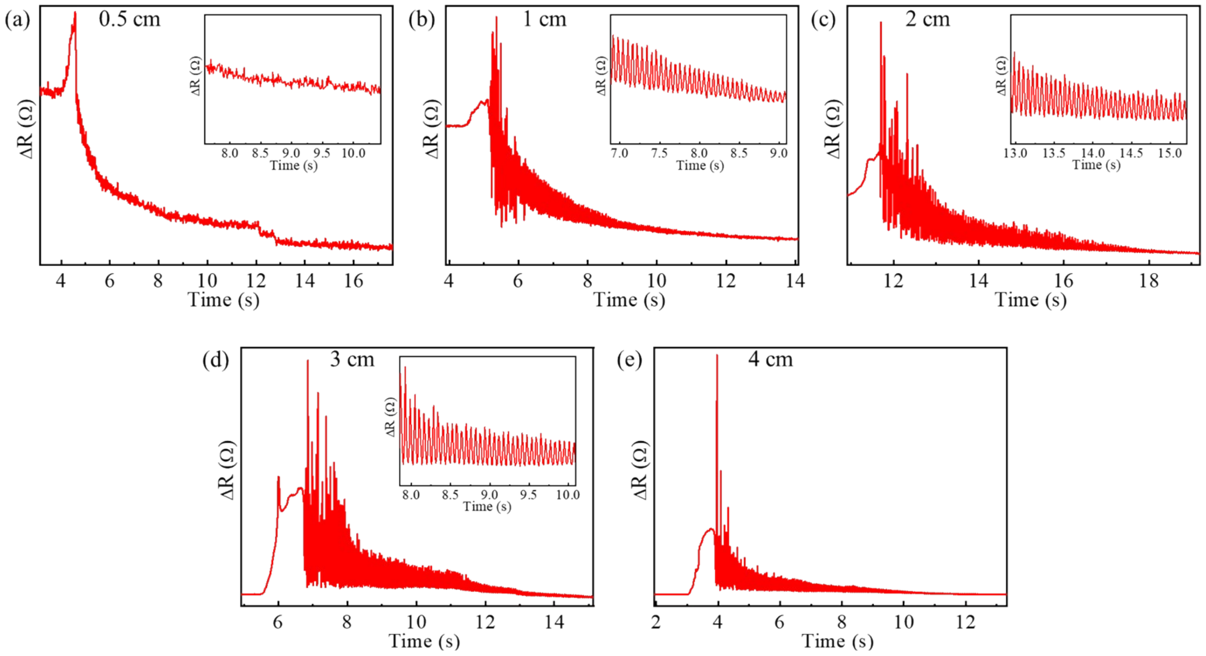

Figure S9. Plots with inset representing resistance change in the device kept at 21 cm cantilever length and subjected to deflection of (a) 0.5, (b) 1, (c) 2, (d) 3, and (e) 4 cm.

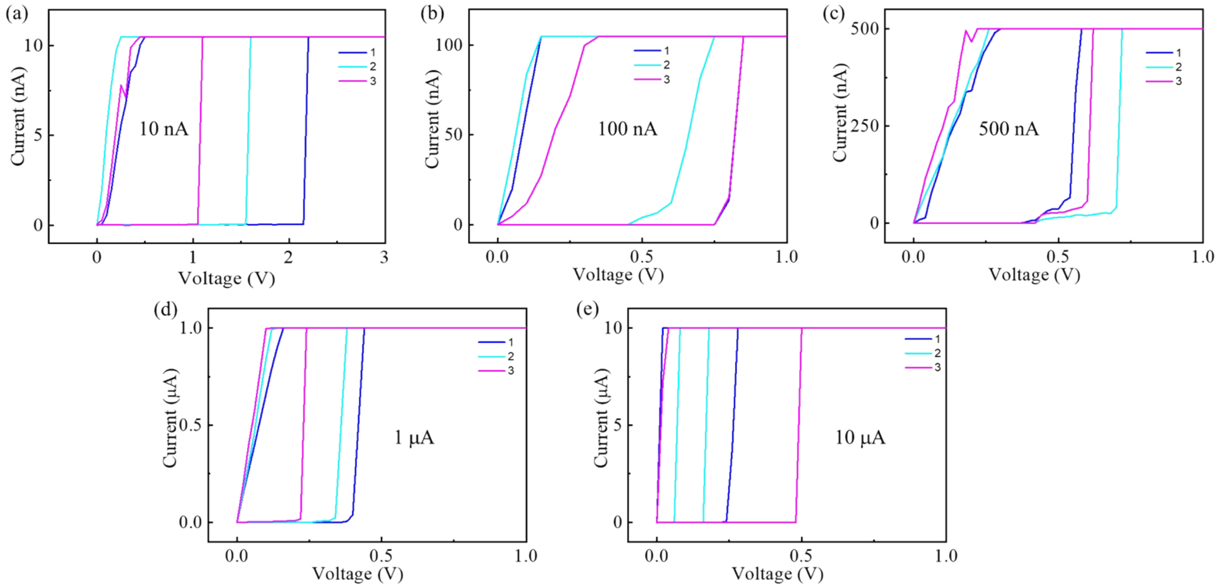

Figure S10. I-V sweeps showing threshold switching at the I_{CC} of (a)10 nA, (b) 100 nA (c) 500 nA (d) 1µA and (e) 10 µA for a ΔS of 0%.

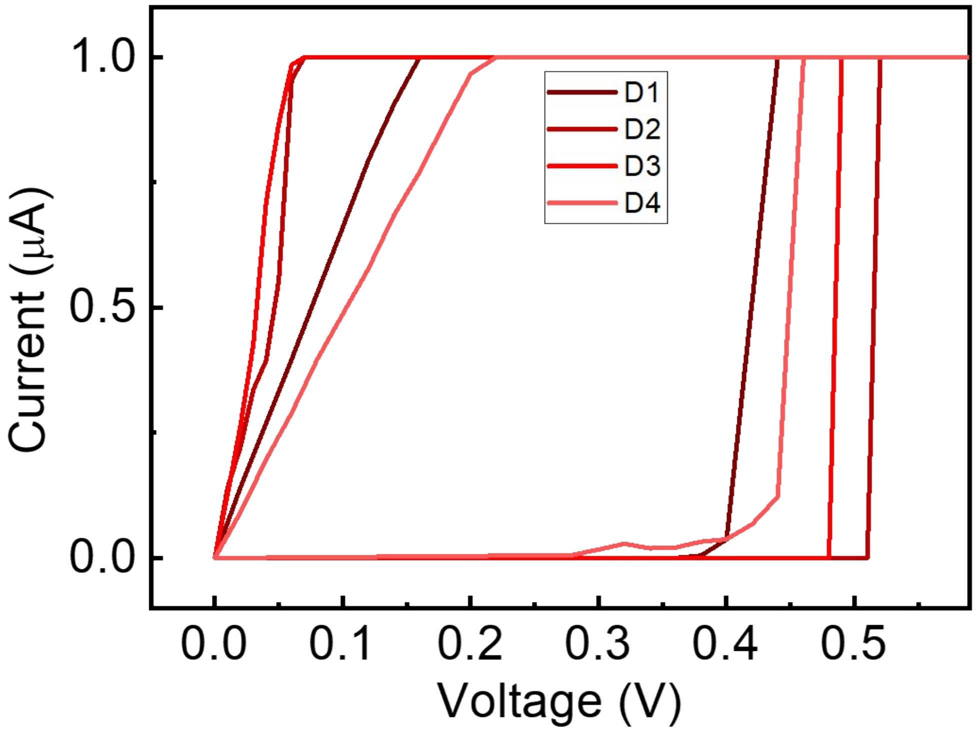

Figure S11. Plot demonstrating device-to-device variability through threshold switching across four distinct neuromorphic devices.

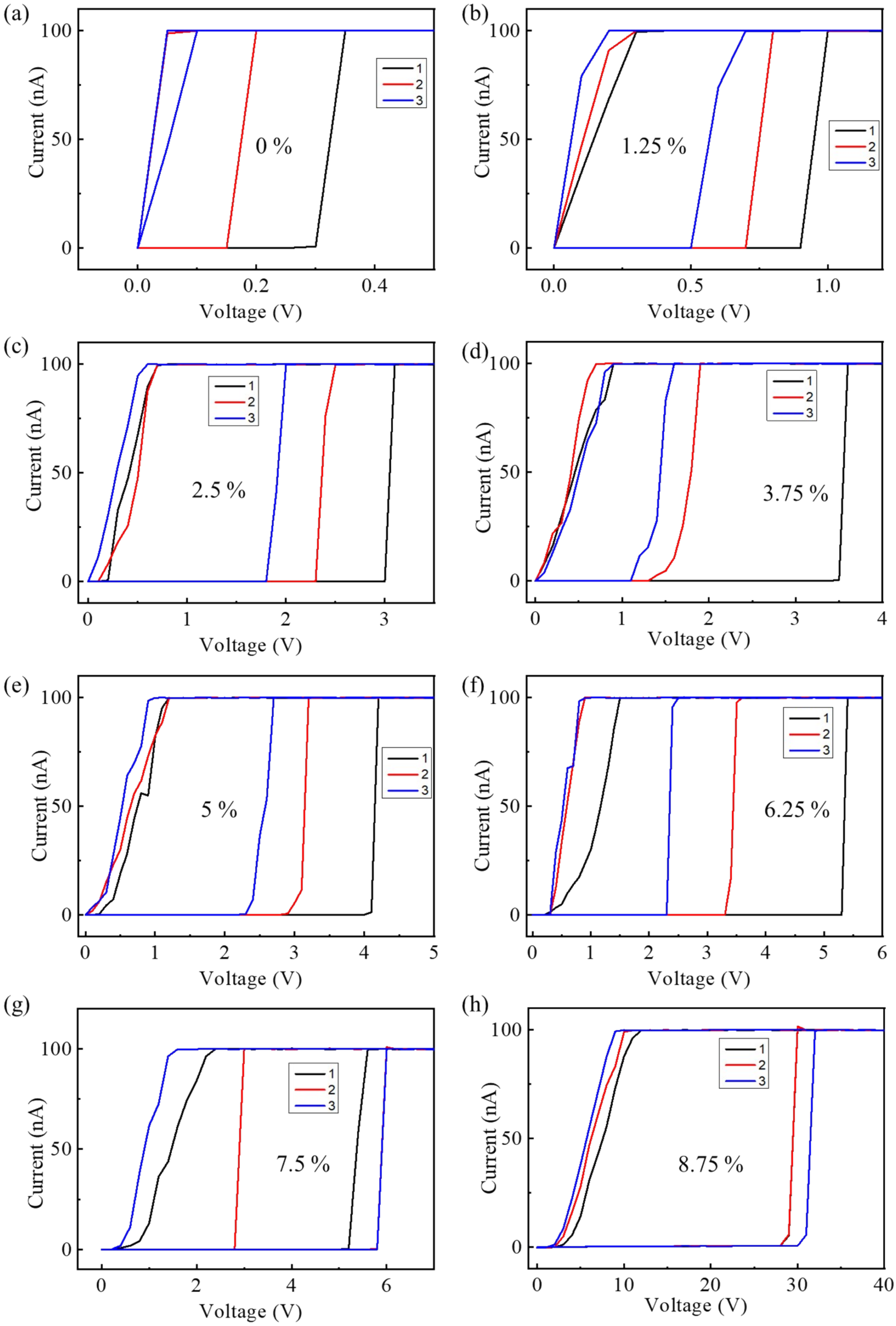

Figure S12. Three consecutive thresholds switching at ΔS of (a) 0% (b) 1.25% (c) 2.5% (d) 3.75% (e) 5.0% (f) 6.25% (g) 7.5% and (h) 8.75%.

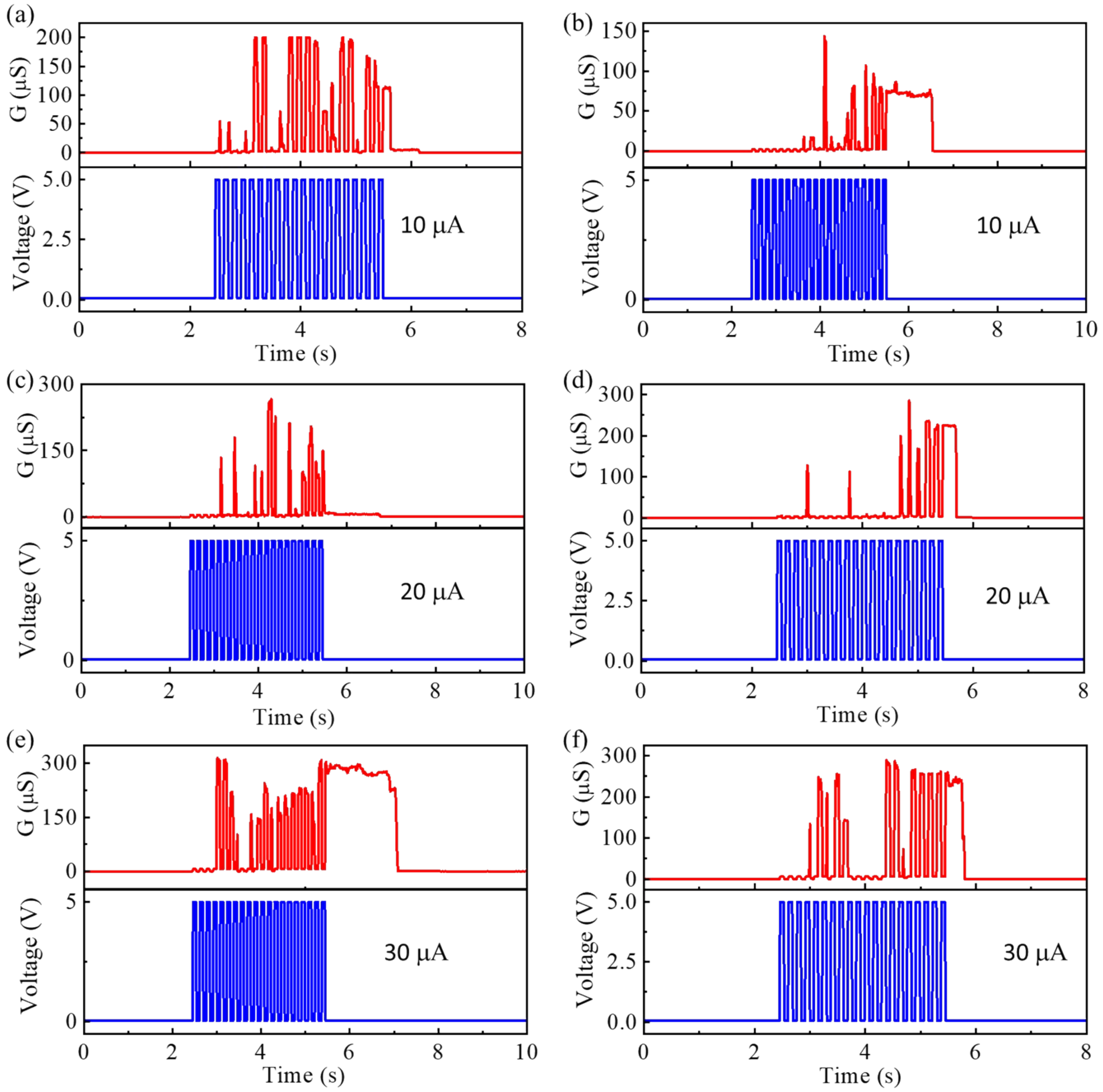

Figure S13. Post-pulsing conductance retention at I_{CC} of (a)-(b) 10, (c)-(d) 20 and (e)-(f) 30 μA.

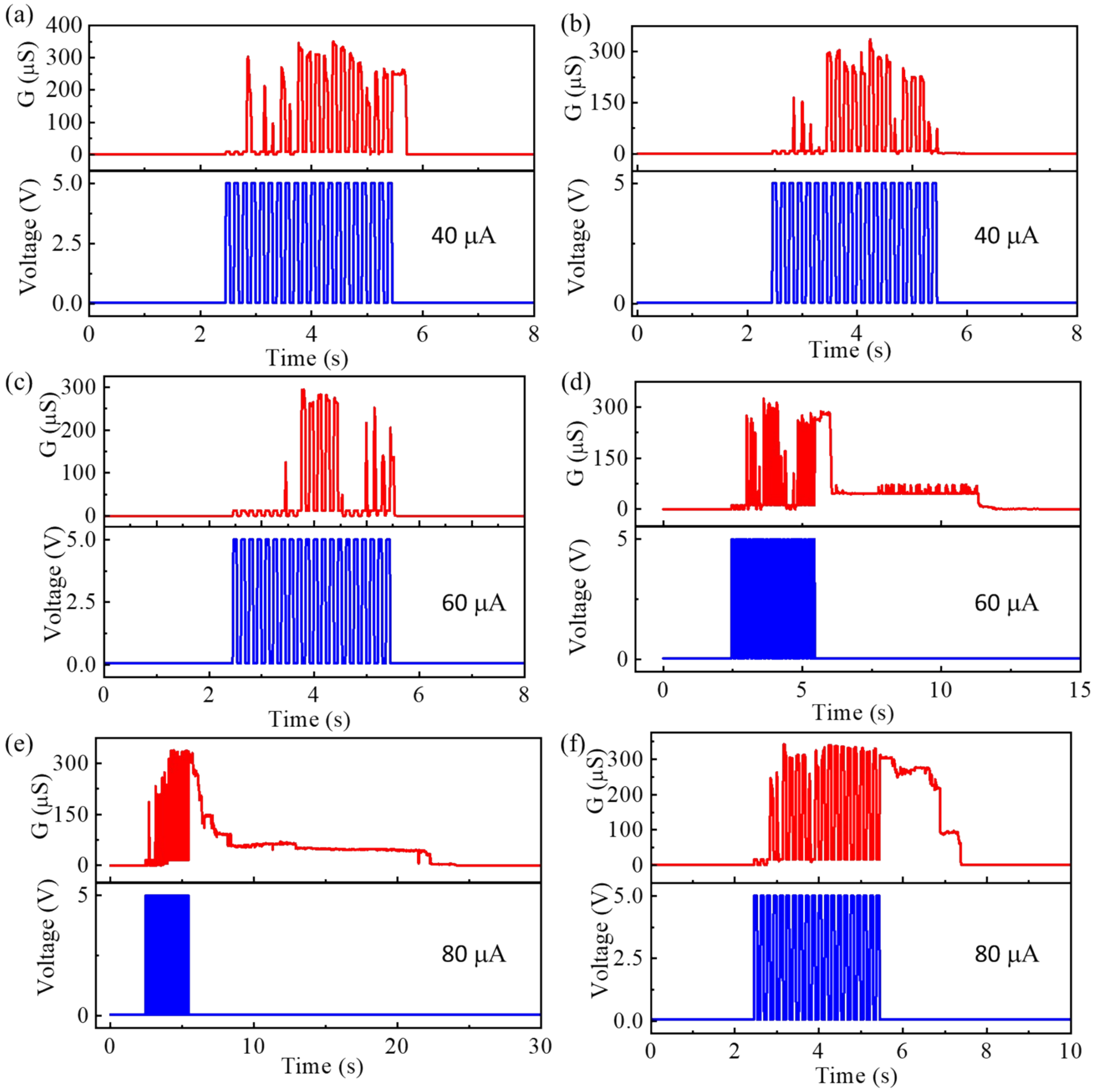

Figure S14. Post-pulsing conductance retention at I_{CC} of (a)-(b) 40, (c)-(d) 60 and (e)-(f) 80 μA.

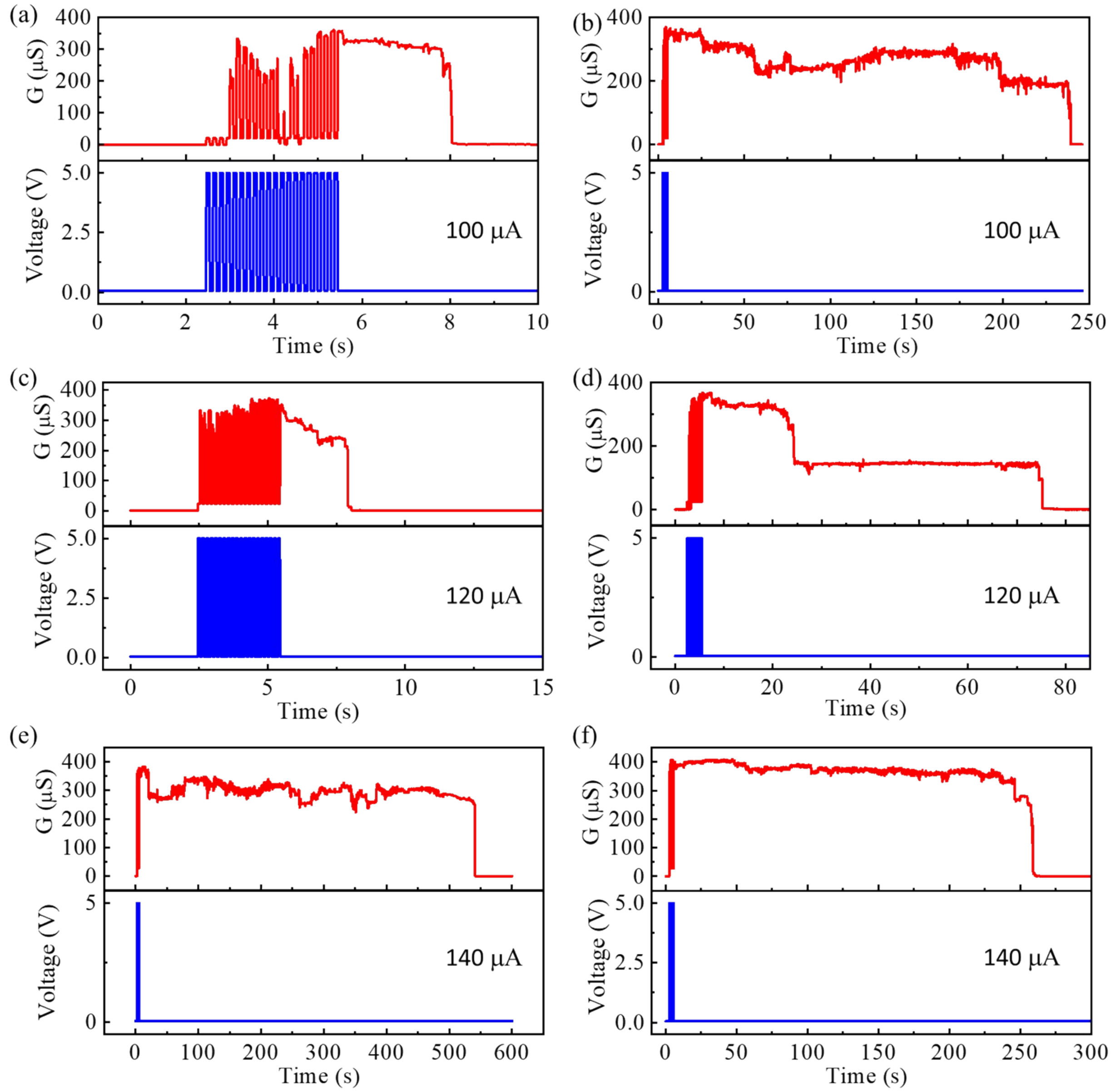

Figure S15. Post-pulsing conductance retention at I_{CC} of (a)-(b) 100, (c)-(d) 120 and (e)-(f) 140 µA.

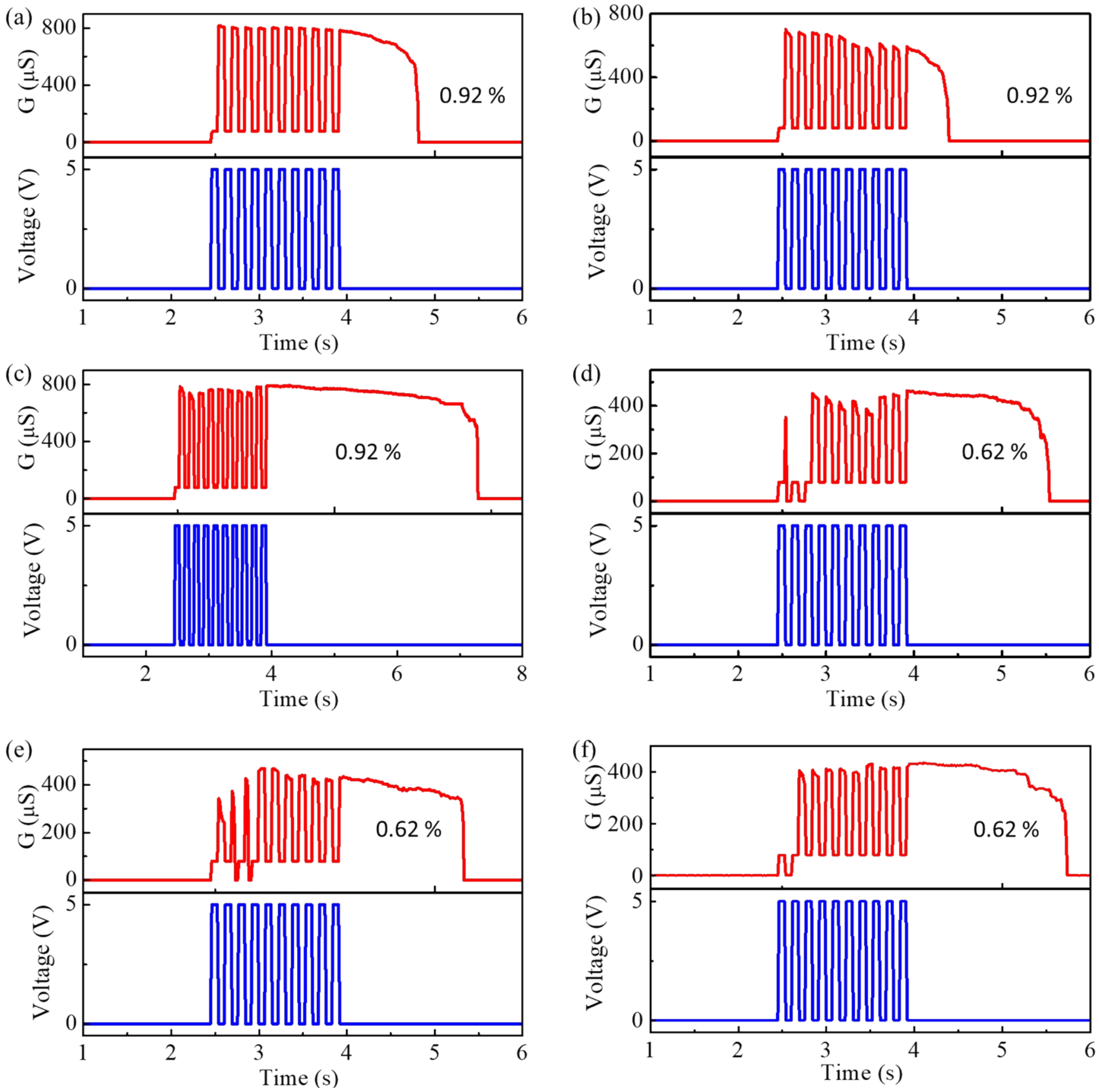

Figure S16. Post pulsing conductance retention at ΔS of (a)-(c) 0.92% and (d)-(f) 0.62%.

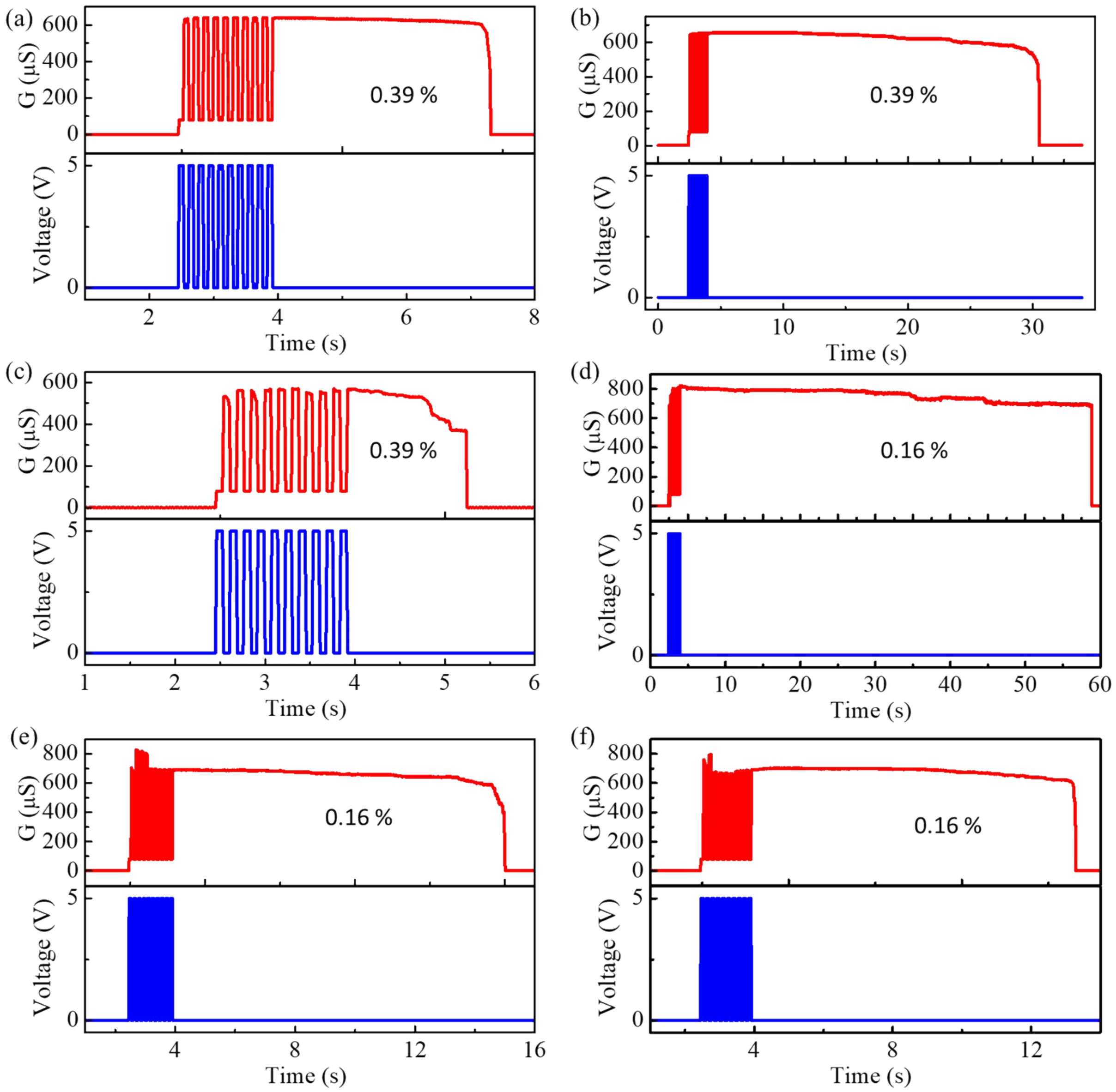

Figure S17. Post-pulsing conductance retention at ΔS of (a)-(c) 0.39% (d)-(f) 0.16%.

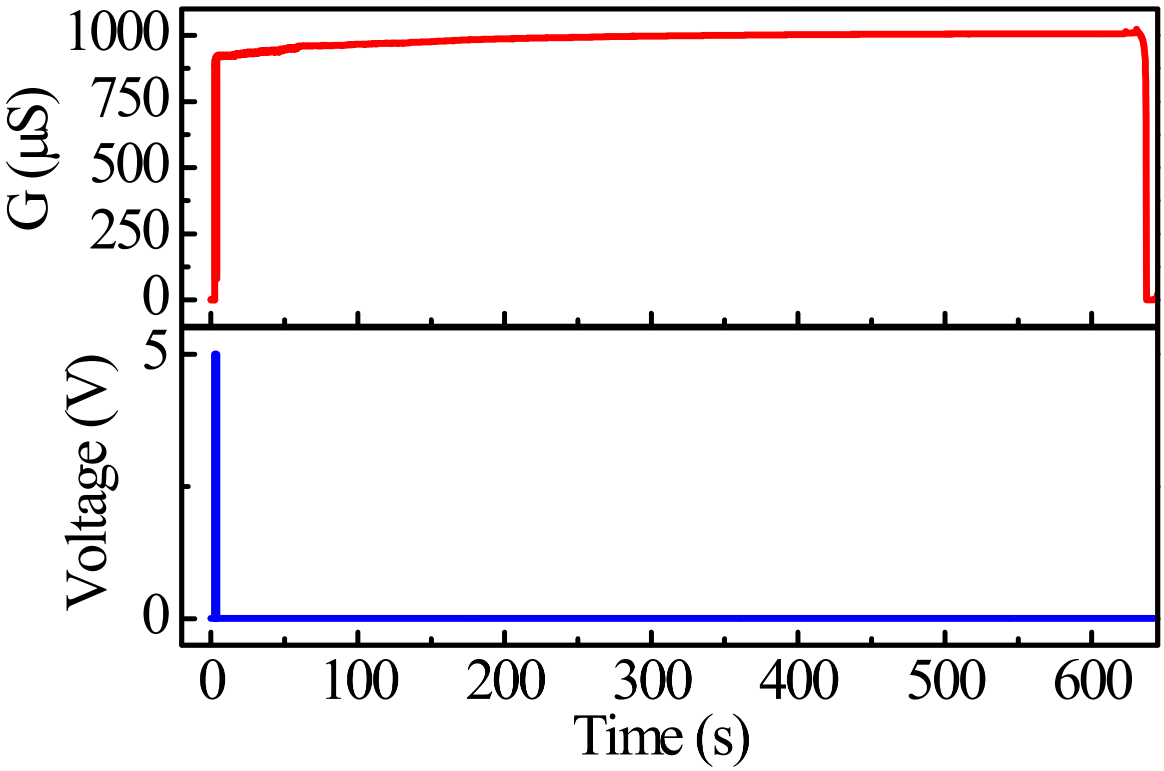

Figure S18. Conductance retention after application of pulse sequence at ΔS of 0%.

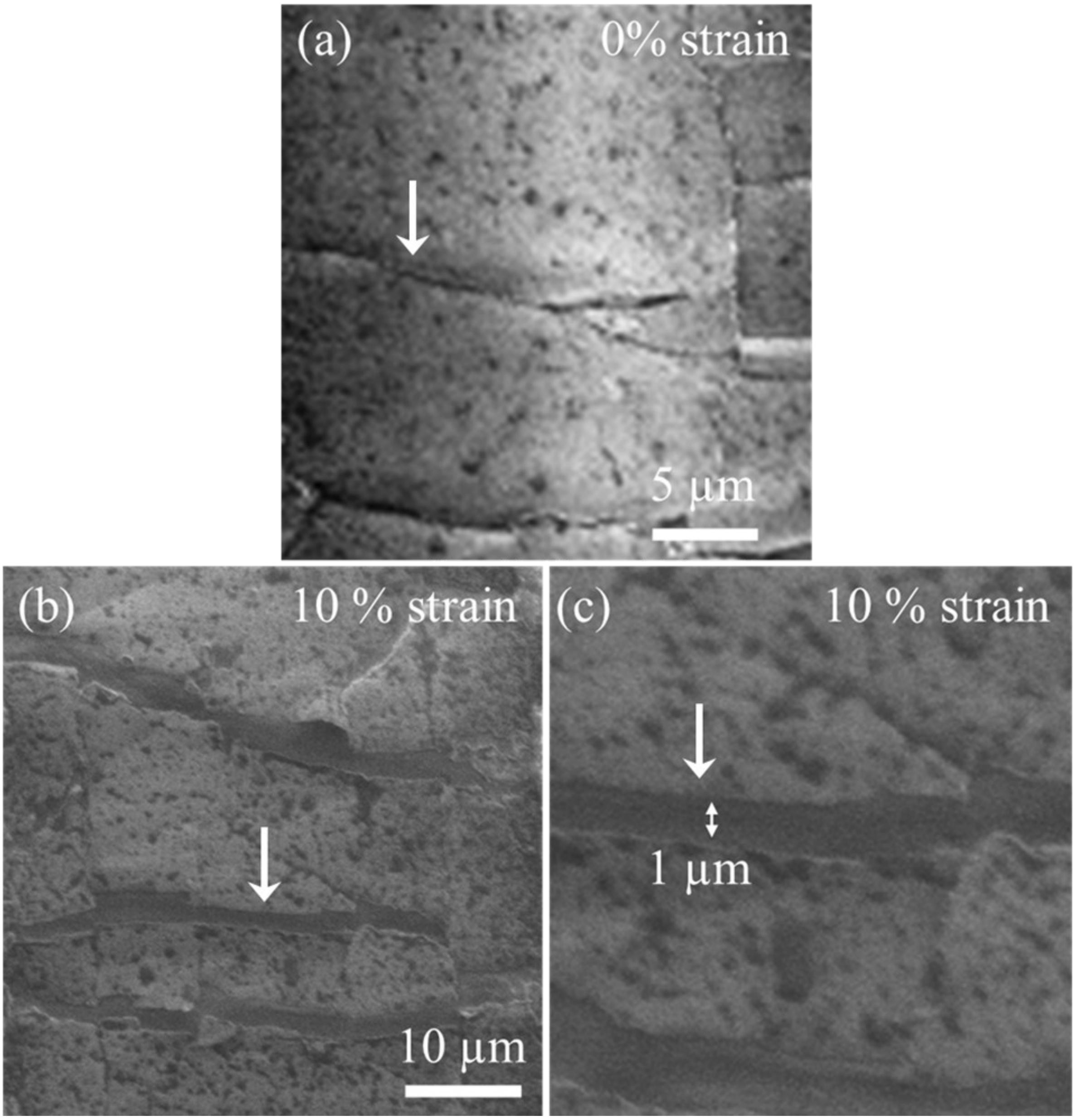

Figure S19. FESEM images of Ag network at (a) 0% strain, (b) and (c) 10% strain. White arrows highlight the development of microstructural gaps as strain is applied.

To enhance the visualization of gaps induced by strain, we applied a higher strain of 10%. The image reveals that the resulting gap is approximately 1 μm. However, under the typical operating conditions of the device, where strain is significantly less than 10%, the gap is expected to be in the range of a few tens to a hundred nanometers depending upon the strain amplitude.

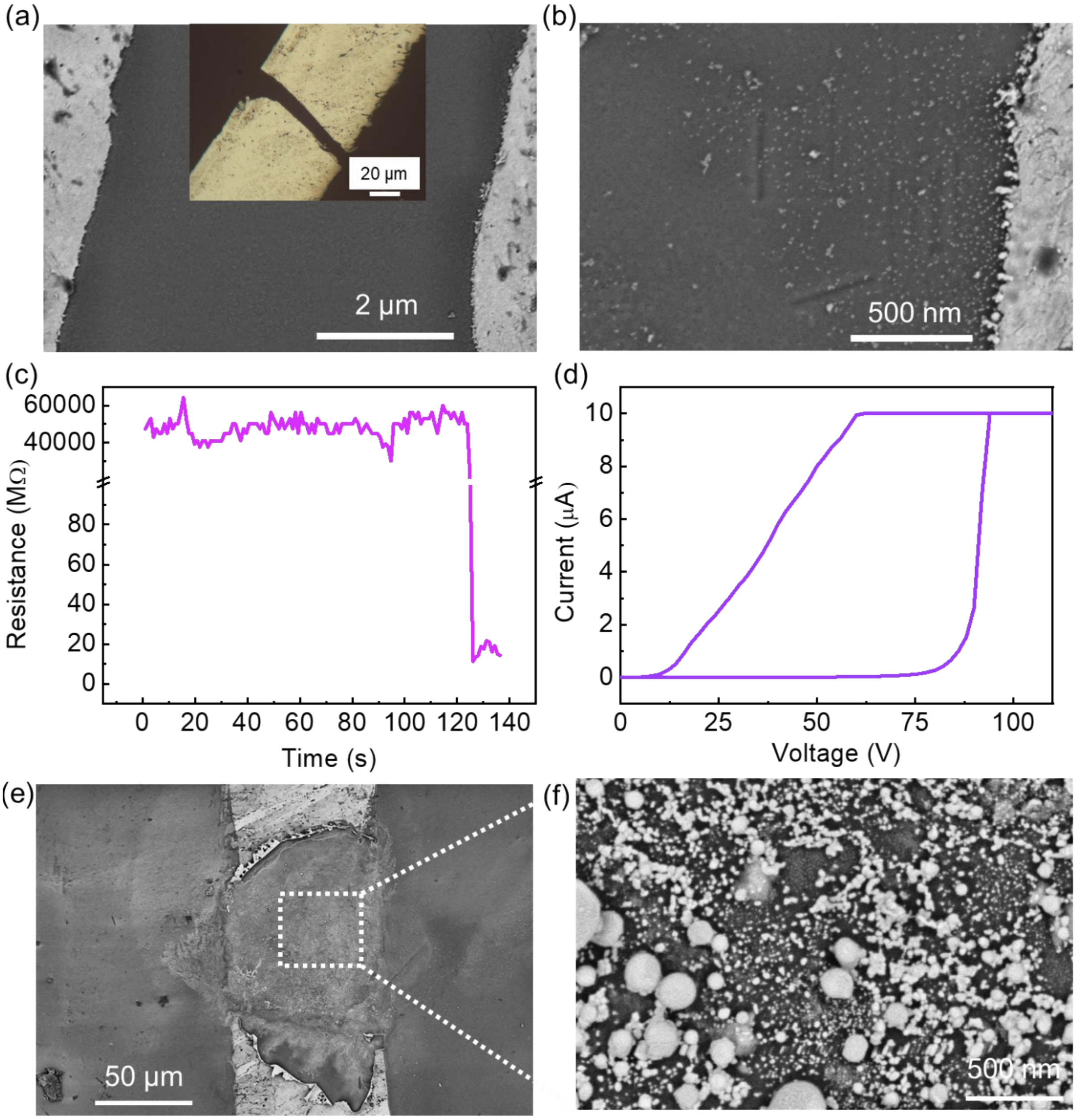

Figure S20. (a) SEM illustrating the gap in the Ag microwire on a glass substrate. Inset shows the optical microscopy image of the same. (b) Zoomed-in image highlighting the gap. (c) Graph depicting resistance variation over time under a 100 V bias at 1 mA I_{CC}. (d) I-V sweep demonstrating the threshold switching behavior in the fabricated device. (e) FESEM image illustrating the widening of the gap after electrical stimulation. (f) Zoomed-in image highlighting the gap, showing traces of silver nanoparticles dispersed across the gap**.**

To confirm the field-induced migration of Ag, we fabricated a similar Ag metal work on a glass substrate (Inset of Figure S20a). We created a narrow scratch to form a gap of approximately 10 µm between the Ag wire (Figure S20a). Zoomed-in SEM image confirms the absence of active material in the gap prior to electrical stimulation (Figure S20b). Two Ag epoxy contacts were used for the electrical measurements. Given that the 10 µm gap had no active material present, a higher voltage was required for the migration. Therefore, the device was subjected to a constant bias of 100 V at 1 mA current. The application of this voltage bias resulted in a change in the device's resistance (Figure S20c). Subsequently, an I-V sweep was performed, showing similar resistive switching as observed in the neuromorphic regime of the stretchable device (Figure S20d). The device was then examined using FESEM to observe the morphological changes after electrical stimulation. The FESEM measurements indicated that applying the electrical bias at 1 mA current resulted in Joule heating of the Ag wire (Figure S20e). The gap increased approximately to 120 μm and zoomed-in images of the gap showed scattered Ag particles due to Ecton fomation (Figure S20f), confirming the migration of Ag under the application of an electric field.

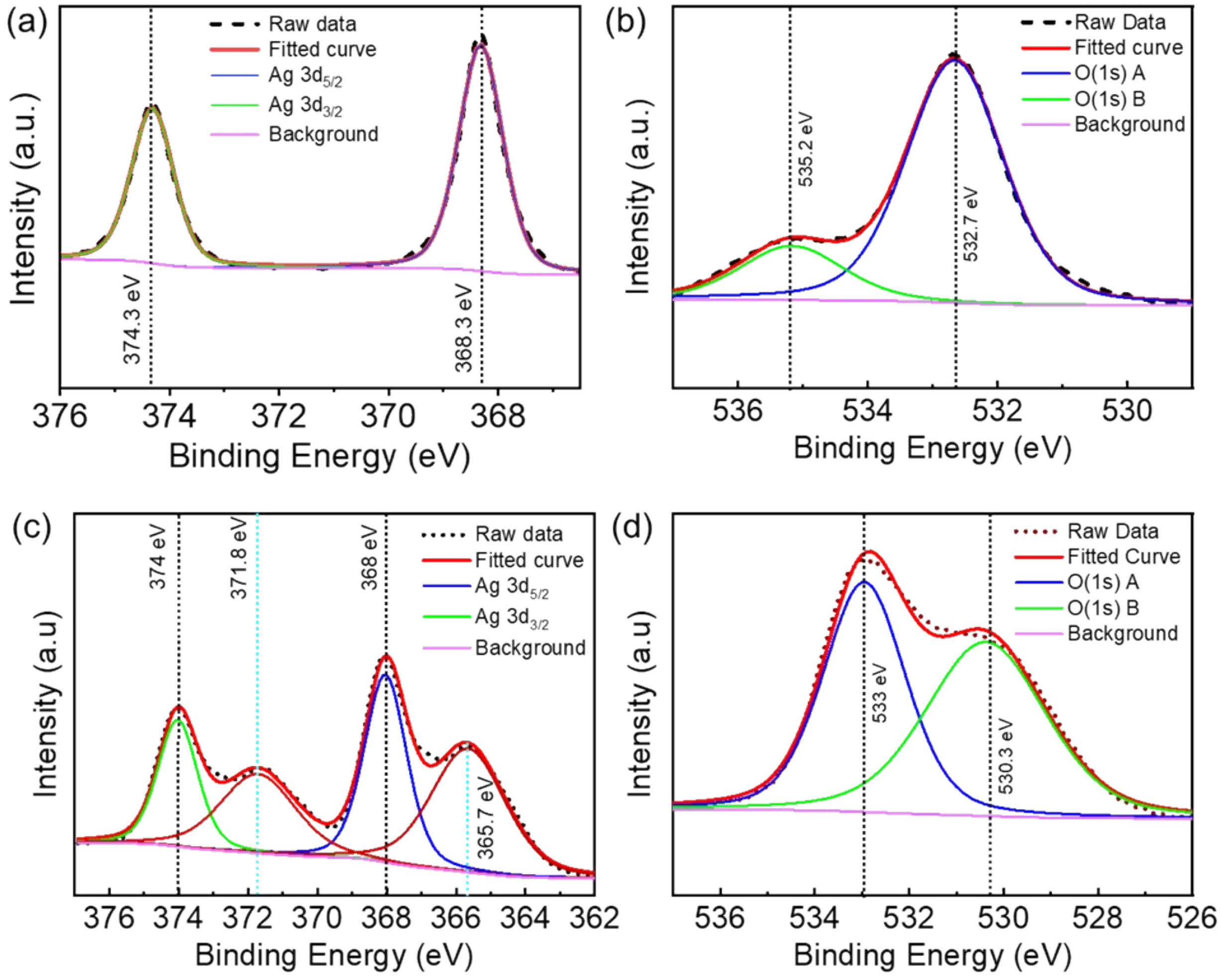

Figure S21. XPS spectra of Ag nanowire on a glass substrate. Pre-pulsing core level spectra of (a) Ag (3d) and (b) O (1s) confirm the presence of metallic Ag. Post-pulsing core level spectra of the (c) Ag (3d) and (d) O (1s) depict the coexistence of metallic and oxidized Ag.

Due to degassing issues under high vacuum, which is required for XPS analysis, it was challenging to perform XPS characterization with the PDMS substrate. However, we fabricated the Ag metal work on a glass substrate and identified a gap where electrical stimulation was applied. XPS analysis was conducted before and after electrical stimulation.

Before stimulation, the XPS spectra showed two peaks for Ag 3d$_{5/2}$ and Ag 3d$_{3/2}$ at approximately 368.3 eV and 374.3 eV, respectively, confirming that the Ag was in its metallic form (Figure S21a)[1]. The O1s peaks did not indicate the presence of metal-oxygen bonds but showed peaks at 535.2 eV due to adsorbed oxygen and at 532.7 eV due to C-O bonding (Figure S21b)[2].

Post-stimulation XPS analysis revealed changes in the chemical state of Ag. Two pairs of peaks for Ag 3d$_{5/2}$ and Ag 3d$_{3/2}$ suggested the coexistence of two different phases of Ag. One pair of peaks at 374 eV and 368 eV corresponded to the metallic phase of Ag, while the other pair at 373.5 eV and 367.5 eV corresponded to oxidized Ag (Figure S21c)[3]. The oxidation of Ag was also reflected in the O1s spectra at 530.3 eV (Figure S21d)[4]. Importantly, even after several cycles of electrical stimulation, the threshold voltage remained nearly constant, indicating the surface oxidation of Ag does not significantly alter the switching mechanism.

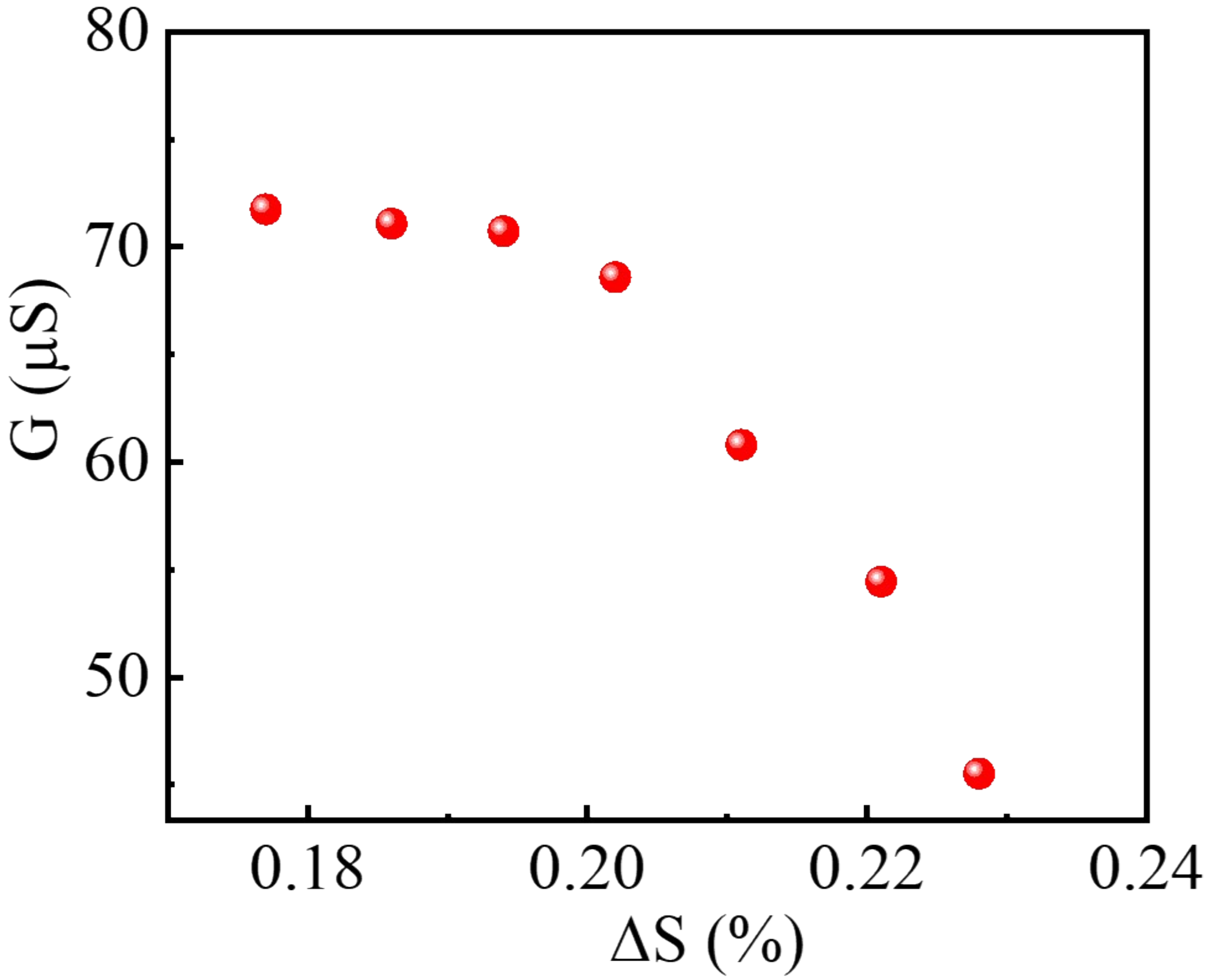

Figure S22. The conductance variation with ΔS in the neuromorphic potentiated regime.

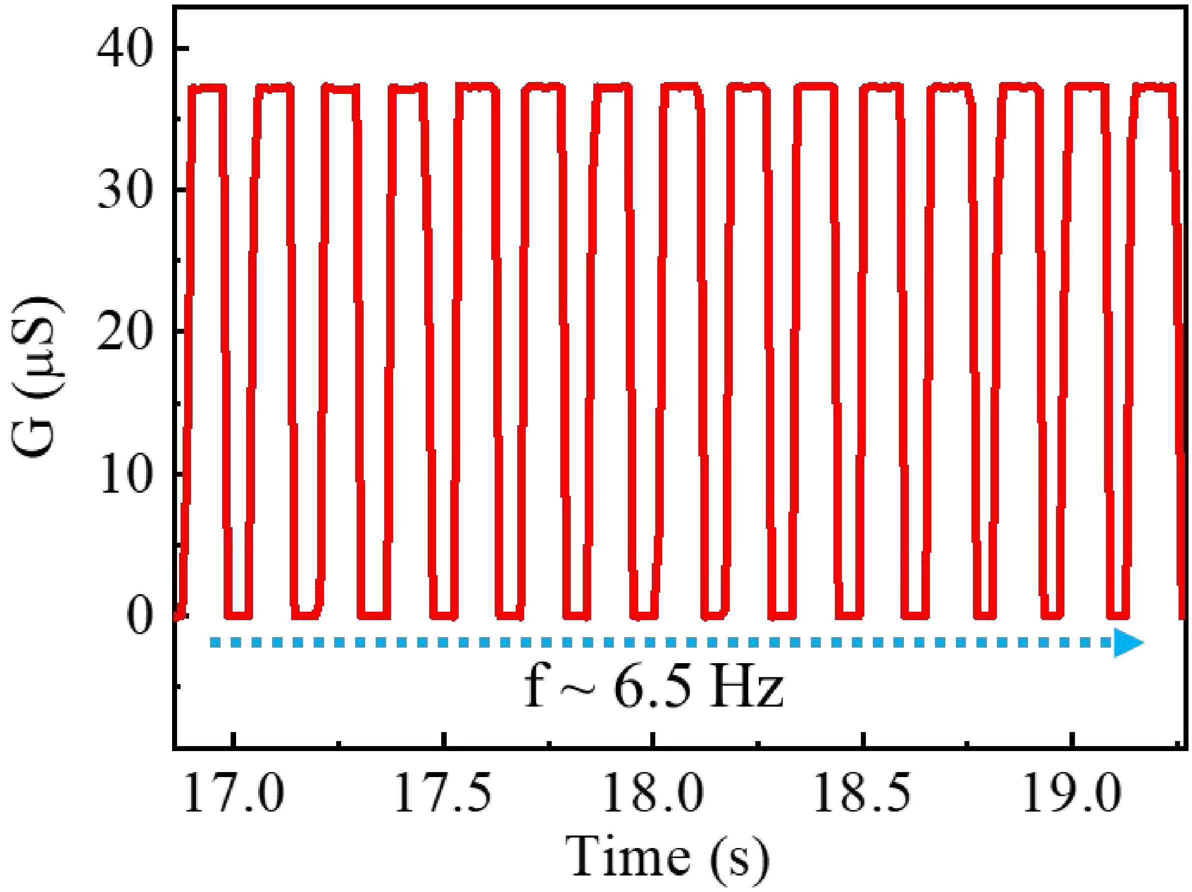

Figure S23. The periodic oscillation of N_{HRS} and N_{LRS} resulted in a frequency of 6.5 Hz.

Note S1: Theoretical frequency of cantilever oscillation was calculated using the equation[5]:

$$\omega = 1.875^2\left(\frac{Eh^2}{12\rho L^4}\right) \text{rad s}^{-1}$$

where E is Young's modulus (Nm^{-2}), h is the thickness of the cantilever (m), ρ is the density of the cantilever-material (kg m^{-3}) and L is the length of the cantilever (m). In the present experiment, the cantilever is a "steel scale" having $E = 2.1 \times 10^{11}$ N m^{-2}, h = 0.00047 m, ρ = 7850 kg m^{-3}, and L = 0.245 m. Therefore, the calculated circular natural frequency for the cantilever beam is.

$$\omega = 41.0 \text{ rad s}^{-1} = 6.52 \text{ Hz}$$

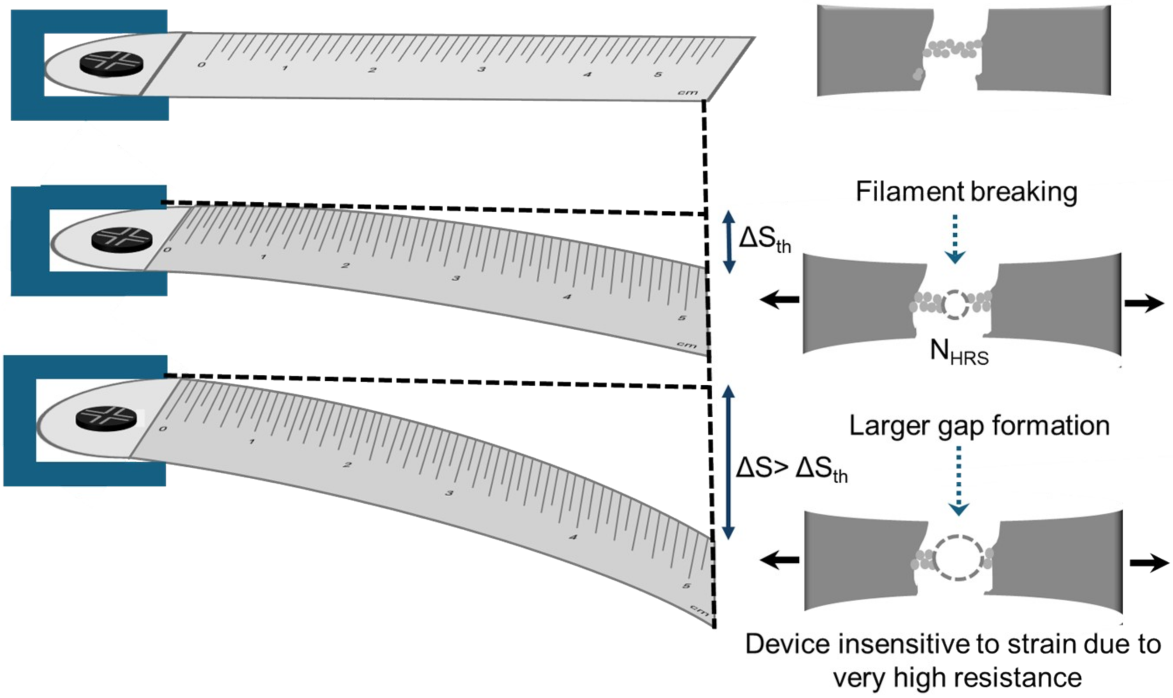

Figure S24. Schematic explanation of the mechanism of the device during oscillatory strain.

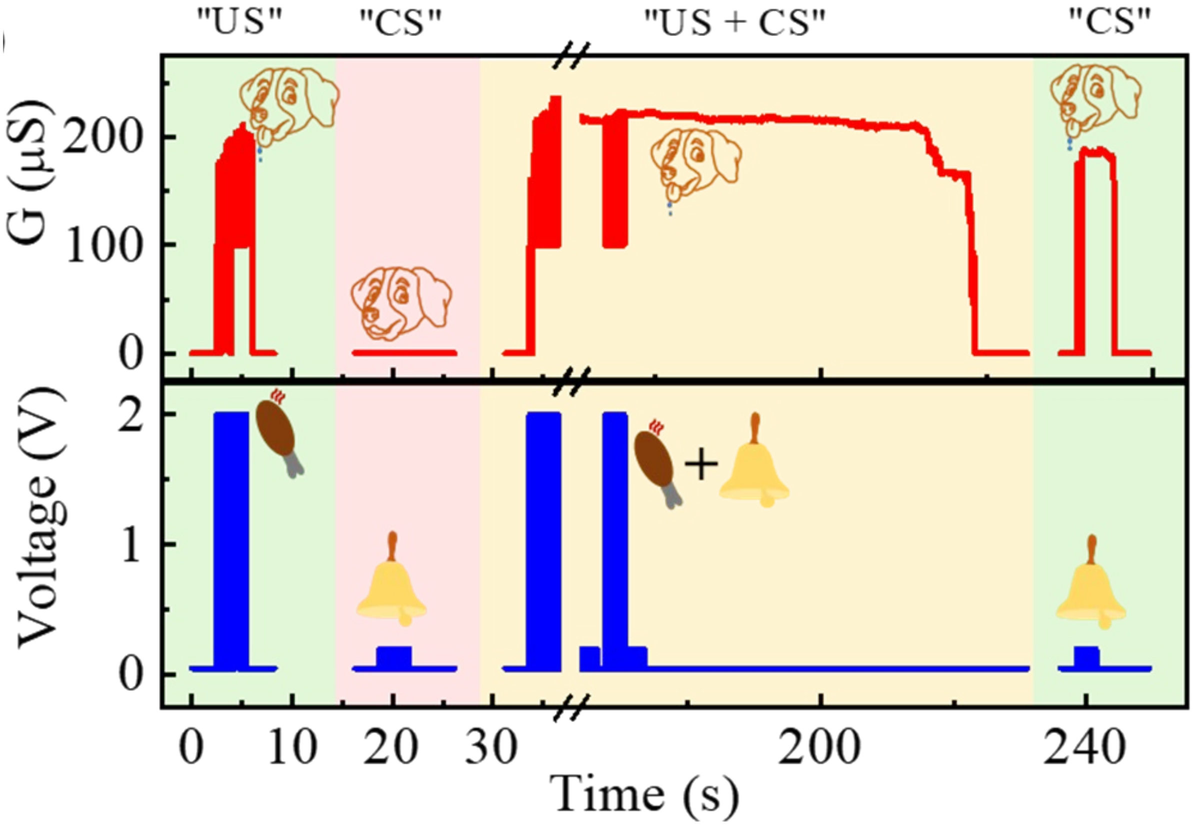

Figure S25. Simulating the classical conditioning by applying 2 and 0.2 V pulses as food and bell, respectively.

Herein, optimum voltage pulses were utilized as food (2 V) and bell (0.5 V) to perform the device-level classical conditioning while monitoring the response using a reading voltage of 50 mV. Food stimulus is the unconditional stimulus (US) which always generates a complete response contrasting to the bell or the conditional stimulus (CS) which is expected to generate a response only after the conditioning. The device was first subjected to a sequence of food pulses which generated a conductance response depicting the unconditional reaction (Figure S25). When the device was subjected to a sequence of bell pulses, no response was observed. Next, 20 sets of food and bell pulse sequences were applied successively. Post-training, the application of bell signals generated the conditional response, indicating a successful emulation of the classical conditioning.

References

1 X. Y. Gao, S. Y. Wang, J. Li, Y. X. Zheng, R. J. Zhang, P. Zhou, Y. M. Yang and L. Y. Chen, *Thin Solid Films*, 2004, **455–456**, 438–442.

2 Y. Liu, H. Jiang, C. Liu, Y. Ge, L. Wang, B. Zhang, H. He and S. Liu, *Atmos. Chem. Phys.*, 2019, **19**, 8175–8187.

3 A. C. Rodrigues, E. L. Da Silva, S. F. Quirino, A. Cuña, J. S. Marcuzzo, J. T. Matsushima, E. S. Gonçalves and M. R. Baldan, *Mater. Res.*, , DOI:10.1590/1980-5373-MR-2018-0530.

4 Z. Golrokhi, P. A. Marshall, S. Romani, S. Rushworth, P. R. Chalker and R. J. Potter, *Appl. Surf. Sci.*, 2017, **399**, 123–131.

5 B. Nie, X. Li, J. Shao, X. Li, H. Tian, D. Wang, Q. Zhang and B. Lu, *ACS Appl. Mater. Interfaces*, 2017, **9**, 40681–40689.